ADVANCED ENERGY MATERIALS
www.advenergymat.de

Double the Capacity of Manganese Spinel for Lithium-Ion Storage by Suppression of Cooperative Jahn–Teller Distortion

Changjian Zuo, Zongxiang Hu, Rui Qi, Jiajie Liu, Zhibo Li, Junliang Lu, Cheng Dong, Kai Yang, Weiyuan Huang, Cong Chen, Zhibo Song, Sicheng Song, Yaoming Yu, Jiaxin Zheng, and Feng Pan**

The relatively low capacity and capacity fade of spinel $LiMn_2O_4$ (LMO) limit its application as a cathode material for lithium-ion batteries. Extending the potential window of LMO below 3 V to access double capacity would be fantastic but hard to be realized, as it will lead to fast capacity loss due to the serious Jahn–Teller distortion. Here using experiments combined with extensive ab initio calculations, it is proved that there is a cooperative effect among individual Jahn–Teller distortions of $Mn^{3+}O_6$ octahedrons in LMO, named as cooperative Jahn–Teller distortion (CJTD) in the text, which is the difficulty to access the capacity beyond one lithium intercalation. It is further proposed that the cationic disordering (excess Li at Mn sites and Li/Mn exchange) can intrinsically suppress the CJTD of $Mn^{3+}O_6$ octahedrons. The cationic disordering can break the symmetry of Mn^{3+} arrangements to disrupt the correlation of distortions arising from individual JT centers and prevent the Mn^{3+}—O bonds distorting along one direction. Interestingly, with the suppressed CJTD, the original octahedral vacancies in spinel LMO are activated and can serve as extra Li-ion storage sites to access the double capacity with good reversible cycling stability in microsized LMO.

1. Introduction

The cathode is generally regarded as the performance-determining component of lithium-ion batteries (LIBs). Ideally, the cathode should deliver high specific capacity, high operating voltage, low cost, superior safety and long cycle life within a wide working temperature range in order to meet the requirements for transportation applications, such as hybrid electric vehicles, plug-in hybrid electric vehicles and pure electric vehicles (PEVs).[1] Among the discovered cathodes, manganese-based lithium manganese spinel oxide, $LiMn_2O_4$ (LMO), is one of the most promising cathode material to meet the above requirements because of its high voltage (≈4.0 V vs Li/Li^+) and low cost.[2] However, the poor cycling performance and the relatively low capacity limit its wide application as a cathode material for LIBs. The poor cycling stability is directly associated with a combination of structural transformation and Mn dissolution driven by the disproportionation reaction of Mn^{3+} and Jahn–Teller (JT) distortion.[3] The relatively low capacity of LMO is attributed to one lithium inserting into the Mn_2O_4 spinel framework (above 3 V).[3b,4] Theoretically, further lithiation to the octahedral vacancies in LMO (by extending the potential window below 3 V) to form over-lithiated $Li_2Mn_2O_4$ would double the capacity, but this is impracticable as it will cause more Mn^{4+} reduced to Mn^{3+} to induce more serious JT distortion, leading to irreversible phase transformation (cubic phase to tetragonal phase) and particle cracks during cycling.[3b,4a,5]

To access the double capacity in LMO, suppression of the severe JT distortion beyond one lithium intercalation is critical. Bulk doping[6] and surface engineering (including surface coating[7] and doping[8]) are two well-developed methods to stabilize the crystal structure and inhibit Mn dissolution to improve the cycling stability for LMO. But they mainly take effect above 3 V and is hard to suppress the severe JT distortion beyond one lithium intercalation below 3 V. So far, only bulk heavy Ti-doping was reported to successfully extend the potential window to 4.95–2.0 V to access double capacity in sub-micron sized $LiMn_{1.0}Ni_{0.5}Ti_{0.5}O_4$, but with significant capacity sacrifice (206.5 mAh g^{-1}) and a modest capacity retention: ≈70% and ≈90% after 50 cycles in the upper (4.95–3.0 V) and lower voltage (3.0–2.5 V) regions, respectively.[9] A partial of tetragonal phase was also formed during cycling in $LiMn_{1.0}Ni_{0.5}Ti_{0.5}O_4$. Thus, other nontraditional methods were developed to access the double capacity of spinel LMO. Lu et al. embedded electrochemically inactive layered Li_2MnO_3 nanodomains into the microsized $LiMn_{1.5}Ni_{0.5}O_4$ to stabilize the crystal structure by accommodating the internal stress from JT distortion,[10] and an extended capacity (≈200 mAh g^{-1}) with good retention (≈90% after 50 cycles) was obtained when cycled between 2 and 4.8 V. It was also reported that morphology control

---

C. Zuo, Z. Hu, R. Qi, J. Liu, Z. Li, J. Lu, C. Dong, K. Yang, W. Huang, C. Chen, Z. Song, S. Song, Y. Yu, Prof. J. Zheng, Prof. F. Pan
School of Advanced Materials
Peking University
Shenzhen Graduate School
Shenzhen 518055, China
E-mail: zhengjx@pkusz.edu.cn; panfeng@pkusz.edu.cn

The ORCID identification number(s) for the author(s) of this article can be found under https://doi.org/10.1002/aenm.202000363.

DOI: 10.1002/aenm.202000363

(e.g., ball milling microsized LMO particles[11] to nanosized particles and synthesis of order mesoporous LMO with nanometer thin walls between the pores[12]) can facilitate the reversible cubic/tetragonal phase transformation during cycling to access the double capacity, but this will decrease the volumetric energy density significantly. Up to date, intrinsic suppression of the severe JT distortion and phase transformation beyond one lithium intercalation in microsized LMO still remains a big challenge.

Here, using experiments combined with extensive ab initio calculations, we report that the double capacity ($\approx$240 mAh g^{-1}) beyond one lithium intercalation can be accessed with good reversible cycling stability by cationic disordering (excess Li at Mn sites and Li/Mn exchange) in microsized spinel LMO in a voltage window of 1.5–4.8 V. Moreover, the capacity in the upper voltage region (4.8–2.8 V) is even increased during cycling. We prove that the cationic disordering can intrinsically suppress the cooperative Jahn–Teller distortion (CJTD) of $Mn^{3+}O_6$ octahedrons (namely, disrupt the correlation of distortions arising from individual JT centers) and inhibit the Mn^{3+} disproportionation in the spinel bulk. With the suppressed CJTD, the original octahedral vacancies in spinel $LiMn_2O_4$ are activated and can serve as extra Li-ion storage sites to access the double capacity.

2. Results and Discussion

Figure 1a shows the XRD patterns of the synthesized spinel $LiMn_2O_4$ with cationic disorder (LMO-CD) and normal $LiMn_2O_4$ spinel. The diffraction peaks of these two kinds of spinel are similar and can be well indexed to the $LiMn_2O_4$ (LMO) standard spinel card (space group = *Fd*-3*m*, PDF#53-1237). The reflected peak of LMO-CD is weaker and broader compared to the normal LMO, indicating an inferior crystallinity. Inductively coupled plasma (ICP) was conducted to determine the exact chemical formula of LMO-CD. The molar ratio of Li/Mn was confirmed to be 0.712 (Table S2, Supporting Information), close to the formula $Li_{1.25}Mn_{1.75}O_4$ according to the stoichiometric lithium manganese spinel formula $Li(Li_xMn_{2-x})O_4$ ($0 < x < 0.33$).[3b,4,13] This indicates that $\approx$25% of octahedral manganese is substituted by lithium in our synthesized LMO-CD. Rietveld refinements were further performed using the *Fd*-3*m* space group by Fullprof, as shown in Figure 1b, and the observed patterns fit well with the calculated patterns with R_{wp} = 8.49%. To our surprise, Li and Mn atoms both have occupancy in 8a and 16d sites, and 8.5% Li/Mn exchange happened in the LMO-CD (Table S1, Supporting Information). Thus, the chemical formula of LMO-CD can be written as $(Li_{0.915}Mn_{0.085})_T(Li_{0.335}Mn_{1.665})_OO_4$ (T and O denote tetrahedral site and octahedral site, respectively). XPS test was conducted to evaluate the valence state of

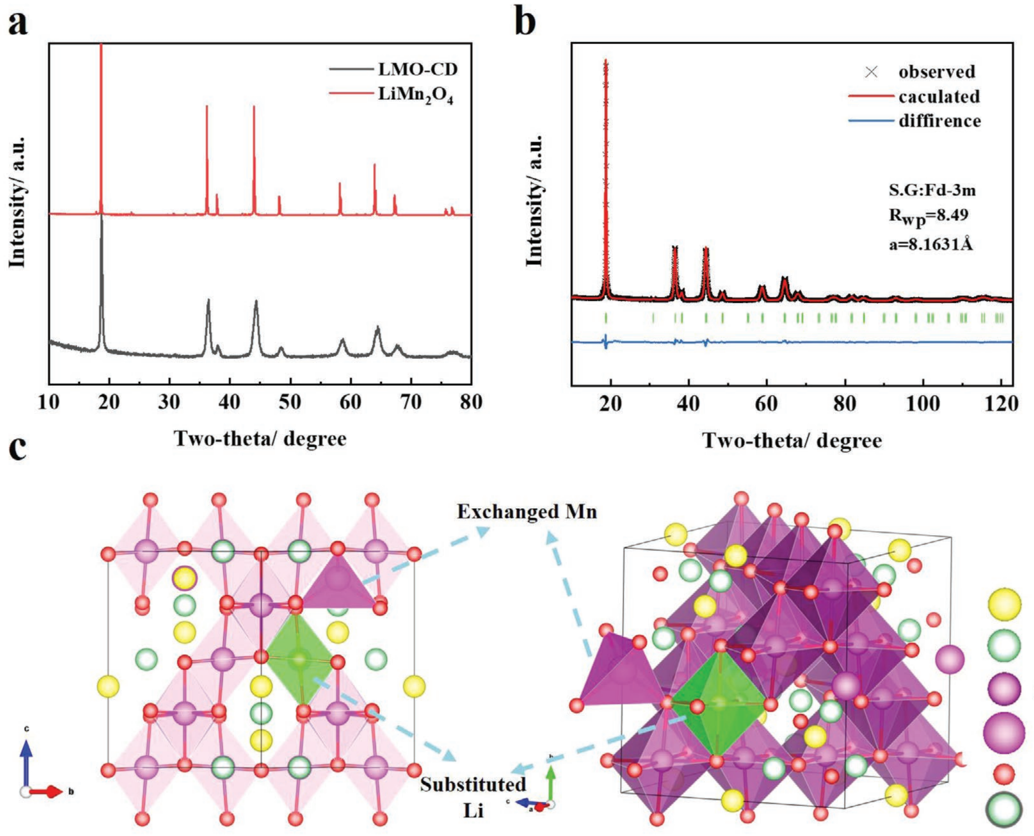

Figure 1. a) XRD patterns of as-prepared normal $LiMn_2O_4$ and LMO-CD; b) Rietveld refinement profiles of XRD for LMO-CD; c) Illustration of crystal structure of LMO-CD sample.

manganese in the sample from the surface to 100 nm depth below the surface by Ar^+ sputtering (Figure S1, Supporting Information). The valence state of Mn on the surface is a little bit lower than that in the bulk. The molar ratio of Mn^{4+}/Mn^{3+} in the bulk was determined as 79.6%/20.4% in LMO-CD (higher than the ratio of 50%:50% in normal LMO), close to the molar ratio of Mn^{4+}/Mn^{3+} in the chemical formula of $(Li_{0.915}Mn_{0.085})_T(Li_{0.335}Mn_{1.665})_OO_4$.

To observe the structure and the morphology, scanning electron microscope (SEM) and high-resolution transmission electron microscope (HRTEM) were employed. Micro-sized particles varied from 1 to 10 µm can be seen from SEM images (Figure S2, Supporting Information). **Figure 2**a,b shows HRTEM images of an LMO-CD particle viewing along the [011] zone axis. Figure 2c–e are magnified areas of three typical regions. As we know, the bright atomic columns in the HRTEM images are the transition metal atoms, while the light elements like lithium are invisible from the images because of the lack of contrast. Therefore, diamond manganese columns marked with red rectangles can be detected in the TEM images (Figure 2d,e), which match with the crystal structure illustration. It can be found that most region of the bulk phase maintains the $LiMn_2O_4$-type spinel structure, in which lithium, manganese, and oxygen occupy the 8a, 16d, and 32e sites, respectively (Figure 2d). Interestingly, the layered-type spinel (Figure 2c–f) was detected in LMO-CD. This is because the normal LMO spinel structure has two kinds of manganese layers: manganese-rich layer and manganese-poor layer. The layer-type spinel region is formed when manganese in the poor layer is substituted by lithium if an amount of lithium is randomly distributed in 16d sites. Inverse manganese was discovered in Figure 2e and can be illustrated by Figure 2h, in which a small amount of tetrahedral manganese was detected in the middle of the red manganese rectangle. Only one tetrahedral spot representing manganese can be found in the manganese diamond framework, which may be due to that two manganese tetrahedrons are not in a plane, namely, only the outward tetrahedron can be observed from the [011] direction.

Electrochemical performance was further tested for the normal LMO and LMO-CD as cathode materials in a voltage window of 1.5–4.8 V. The first charge and discharge curve of LMO-CD and normal LMO at a current density of 50 mA g^{-1} are displayed in **Figure 3**a. Two typical platforms at 4.1 and 2.8 V can be observed from the discharge curve of normal LMO, corresponding to the lithiation into the 8a (tetrahedron sites) and 16c (original octahedron vacancy sites in LMO) sites.[3b] By contrast, three plateaus at 4.0, 2.8, and 2.1 V were observed in LMO-CD. Platform at 4.0 V indicating the lithium inserting into the tetrahedron sites is similar to the normal LMO. The other two low platforms result from the lithiation into the original octahedron vacancy sites in LMO-CD, which will be discussed in detail in the computational section. The

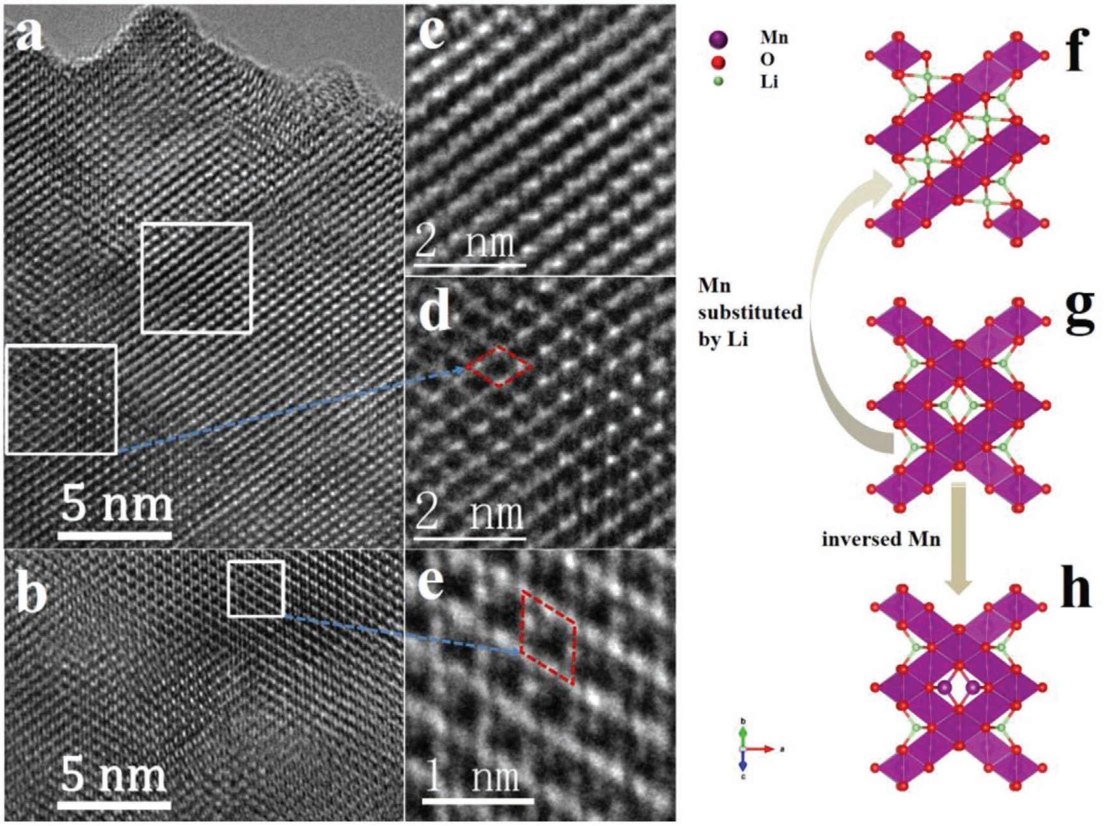

Figure 2. a,b) HRTEM images of LMO-CD particle along the [011] zone axis. Typical areas are marked by white rectangles and the corresponding regions are shown in c) substituted layered-like region, d) normal spinel region and e) manganese inversed region. f–h) Atomic crystal structure illustrations of three typical areas in LMO-CD.

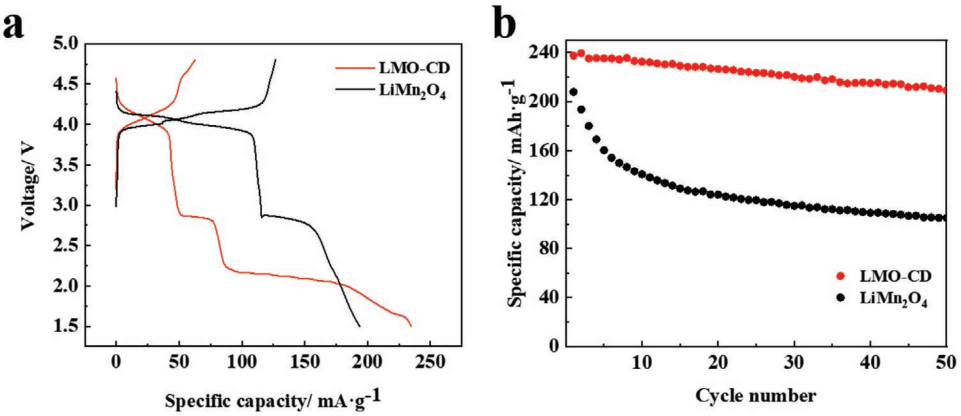

Figure 3. a) 1st charge/discharge curves for LMO-CD and normal $LiMn_2O_4$ at 50 mA g^{-1} current density in a voltage window of 1.5–4.8 V; b) cycle stability test for LMO-CD and normal $LiMn_2O_4$.

cycle voltammetry curves of LMO-CD is shown in Figure S4a (Supporting Information), and the CV peaks match well with the three platforms in charge and discharge curves. The two peaks around 4 V may be caused by the two-phase transition stages and polarization.[14] The initial specific charge capacity for LMO-CD is only 60 mAh g^{-1}, much lower than that of normal LMO (≈110 mAh g^{-1}). This is limited by the charge transfer amount of Mn ions from an average of 3.8 to 4.0 valence state in LMO-CD. The initial specific discharge capacity of LMO-CD is about 240 mAh g^{-1}, much higher than that of normal LMO (200 mAh g^{-1}). These results indicate that both normal LMO and LMO-CD are overlithiated when discharging to low voltages after the initial cycle, and the chemical formula can be figured out as $Li_{2.115}(Mn_{0.085})_T(Li_{0.335}Mn_{1.665})_OO_4$ and $Li_2Mn_2O_4$ at the end of discharge state for LMO-CD and normal LMO, respectively. After 50 cycles at the current density of 50 mA g^{-1}, the capacity retentions of LMO-CD is 87.5% with coulombic efficiency closed to 100% (Figure S5, Supporting Information), indicating a stable reversibility of overlithiated LMO-CD at the voltage window of 1.5–4.8 V (Figure 3b). More importantly, the capacity in the upper voltage region (4.8–2.8 V) is even increased during cycling (Figure S5, Supporting Information). By contrast, the capacity retentions of normal LMO is only 50.2%, indicating a poor reversibility of overlithiated normal LMO (Figure 3b). Furthermore, we match our LMO-CD cathode with a prelithiated SiO/C anode which is prepared by disassembling the lithiated SiO/C in a half cell (vs Li^+/Li) to assemble a full cell. Figure S7 (Supporting Information) shows the corresponding electrochemical performance of this full cell in the voltage window of 1.4–4.7 V. It shows similar electrochemical curves with LMO-CD half cells despite some decomposition of electrolyte in the first cycle. From Figure S7a (Supporting Information), it can be seen that the lacked lithium in the first charge cycle is successfully compensated in the next cycle. Figure S7b (Supporting Information) shows the cycling performance of this full cell. There is nearly no decay after 30 cycles, demonstrating the good cycle stability of the LMO-CD full cell.

In order to understand structure-stability relationship of LMO-CD, ex situ XRD analysis was carried out at different charge-discharge potential, in which half cells were disassembled to further investigate LMO-CD. **Figure 4**a shows the ex situ XRD patterns of LMO-CD at different discharge states, related to each potential shown in Figure 4b. As can be seen, except for some peaks reflected by carbon, blender and Al foil, the spinel framework marked by arrows is well maintained during charge and discharge, especially when discharged to a relatively low voltage. Cell volume and the value of cell parameter c/a of LMO-CD which can be used to describe the level of the JT effect (Figure 4c). It shows that the cell volume went through a relatively smaller change ranging from 531.66 to 546.52 Å^3 and c/a value of LMO-CD was kept almost at the cubic level when discharged from 4.8 to 1.8 V. While the cell volume and c/a value of normal LMO underwent a significant increase after 3.5 V during the discharge process, indicating the significant JT distortion during cycling. Similar results can also be observed by discharging both normal LMO and LMO-CD to 1.8 V at which most Mn^{4+} is reduced to Mn^{3+}. Figure 4d shows the XRD patterns of both normal LMO and LMO-CD when discharged to 1.8 V at which most Mn^{4+} is reduced to Mn^{3+}. It can be seen that the cubic normal LMO structure was almost transformed to tetragonal $Li_2Mn_2O_4$ with (111) peak splitting and the occurrence of typical tetragonal peaks, resulting from the JT distortion. This explains the nonreversibility of overlithiated normal LMO in the cycling voltage window of 1.5–4.8 V. By contrast, for the LMO-CD, despite the reflection of acetylene black and blinder, little tetragonal peaks can be detected in XRD patterns, indicating a well retained cubic spinel symmetry. To prove the reversibility of the LMO-CD cathode in the following cycles, we collected ex situ XRD of LMO-CD and traditional $LiMn_2O_4$ after more cycles (3 cycles, 7 cycles, and 10 cycles, respectively). As shown in Figure S6 (Supporting Information), the main peak of traditional $LiMn_2O_4$ around 18.7° splits off with the emergence of some $Li_2Mn_2O_4$ tetragonal phase peaks, indicating the phase transformation from cubic to tetragonal phase due to the severe cooperative Jahn–Teller distortion in traditional LMO. While LMO-CD showed a much more reversible structure with the main peak staying intact and the spinel framework maintaining stable after 10 cycles, which demonstrate the good reversibility of LMO-CD and the suppression of cooperative Jahn–Teller effect. Furthermore, our TEM measurements also confirm the cycle stability of LMO-CD (Figure S3,

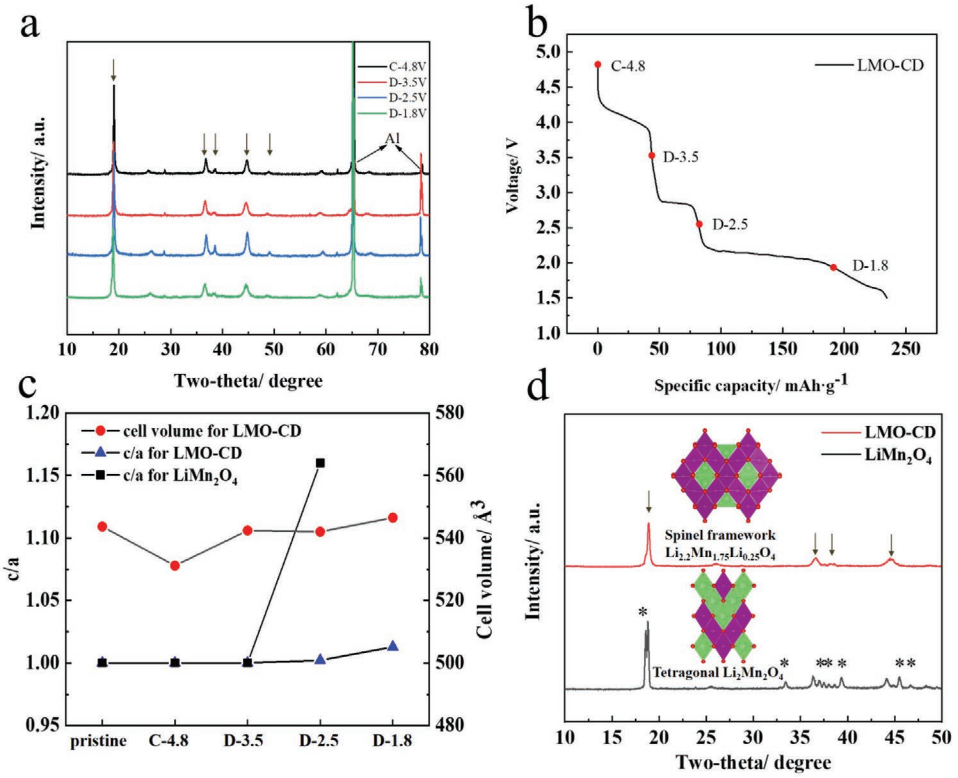

Figure 4. a) Ex situ XRD pattern for LMO-CD at different charge-discharge potentials. Spinel framework reflections are marked. b) Ex situ XRD position in the first curve of LMO-CD corresponding to (a); c) Cell volume and c/a change for LMO-CD and normal $LiMn_2O_4$ at different charge-discharge potentials; d) XRD patterns for the two samples when discharged to 1.8 V (overlithiated LMO-CD and normal LMO). The spinel framework and tetragonal phase were marked.

Supporting Information). Therefore, the JT effect was significantly suppressed in LMO-CD due to the lithium enrichment, and the original octahedral vacancies in LMO-CD can serve as extra Li-ion storage sites with good reversible cycling stability because of the suppressed JT effect.

To get a deep insight into the cationic disordering effect in LMO-CD, the structure, thermodynamic properties, and electronic structure were studied by ab initio calculations. The structure of LMO-CD ($(Li_{0.915}Mn_{0.085})_T(Li_{0.335}Mn_{1.665})_OO_4$) was constructed by substituting two 16d Mn ions with Li-ions and exchange position between one 8a Li-ion and one 16d Mn-ion from normal spinel LMO. Enumerated configurations with exchange position constructed from $(Li_{0.915}Mn_{0.085})_T(Li_{0.335}Mn_{1.665})_OO_4$ were calculated, and then the lowest energy configuration was determined. It should be noted that according to the experimental results, excess Li-ions facilitate Li/Mn exchange in LMO-CD. The calculated formation energy of per Li/Mn exchange with excess Li-ions is lower than that of normal LMO by 0.66 eV (Table S3, Supporting Information), which confirms the experimental results. The structure of over-lithiated $Li_{2.115}(Mn_{0.085})_T(Li_{0.335}Mn_{1.665})_OO_4$ was built by redistributing excess Li ions in the tetrahedral 8a and the octahedral 16c sites based on $(Li_{0.915}Mn_{0.085})_T(Li_{0.335}Mn_{0.665})_OO_4$ obtained from the previous step. By comparing the energies of different Li arrangements, we found that Li ions prefer to be accommodated at octahedral 16c sites when additional Li ions were added in this system.

We start our analysis on the ground-state Li/vacancy configurations and voltage profiles versus Li concentration. The thermal stability of the Li-extraction was determined by the formation energies, which were calculated with respect to the end members $(Mn_{0.085})_T(Li_{0.335}Mn_{1.665})_OO_4$ and $Li_{2.115}(Mn_{0.085})_T(Li_{0.335}Mn_{1.665})_OO_4$ according to the following formula

$$
\begin{aligned}
E_f = {} & E\left[\mathrm{Li}_x\,(\mathrm{Mn}_{0.085})_T\,(\mathrm{Li}_{0.335}\mathrm{Mn}_{1.665})_O\,\mathrm{O}_4\right] - \\
& \frac{x}{2.115}E\left[\left[\mathrm{Li}_{2.115}(\mathrm{Mn}_{0.085})_T(\mathrm{Li}_{0.335}\mathrm{Mn}_{1.665})_O\mathrm{O}_4\right]\right] - \\
& \frac{(2.115-x)}{2.115}E\left[(\mathrm{Mn}_{0.085})_T\,(\mathrm{Mn}_{1.75}\mathrm{Li}_{0.25})_O\ \mathrm{O}_4\right]
\end{aligned}
\tag{1}
$$

Where E is the total energy of the particular configuration marked in a square bracket with x delithiation fraction, E_f represents the formation energy for this configuration. Three stable intermediate ground states are predicted at $x = 0.55$ (25%), 0.825 (37.5%), and 1.1 (50%). The convex hull obtained from formation energies is presented in **Figure 5**a. Considering the charge process (delithiation process) with over-lithiated $Li_{2.115}(Mn_{0.085})_T(Li_{0.335}Mn_{1.665})_OO_4$ as the initial state, the convex hull shows that delithiation initially occurs via a two-phase separation from $Li_{2.115}(Mn_{0.085})_T(Li_{0.335}Mn_{1.665})_OO_4$ toward $Li_{1.015}(Mn_{0.085})_T(Li_{0.335}Mn_{1.665})_OO_4$ phase. At $x = 1.65$ (75%), all lowest-energy configurations prefer 16c octahedral occupation with formation energies very close to convex hull, which indicates a weak two-phase transition for

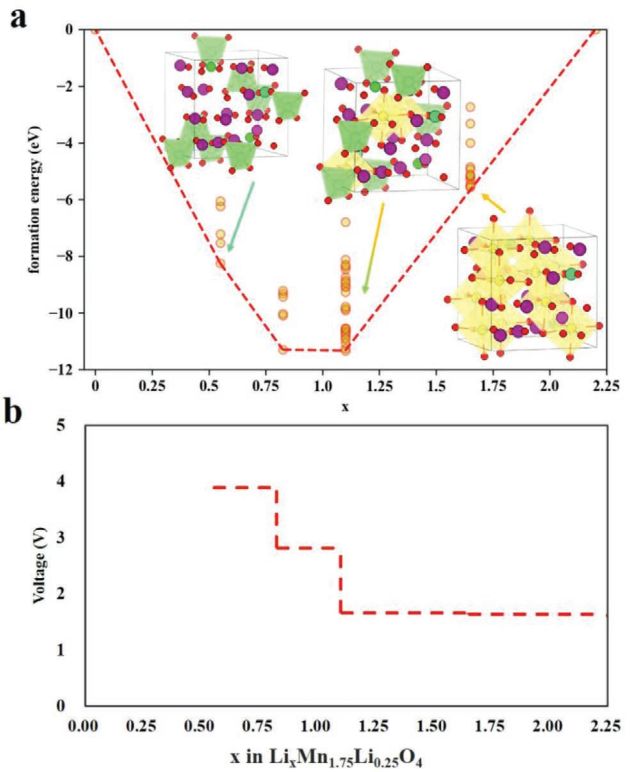

Figure 5. a) The formation energies of all the configurations considered (orange open circles) and the convex hull for the delithiation of $Li_{2.115}(Mn_{0.085})_T(Li_{0.335}Mn_{1.665})_OO_4$ (orange line). Formation energies are presented with per supercell of $(LixMn_{0.085})_T(Li_{0.335}Mn_{1.665})_OO_4$. The inset shows the supercells relaxed for percentage of delithiation at 25%, 37.5%, and 50%. Yellow represents 16c octahedral sites and green represents 8a tetrahedral sites. b) The average voltage curve obtained from convex hull.

$1.015 < x < 2.115$. At $x = 1.015$ (50%), the lowest energy structure prefers to accommodate Li ions into 8a tetrahedral and 16c octahedral sites simultaneously. At this Li extraction stage, Li ions tend to occupy 16c octahedral sites, Li ions are removed from 16c octahedral sites and then Li-ions redistribute in both tetrahedral and octahedral sites. At $x = 0.74$ (37.5%), 8a tetrahedral sites are favorable sties to accommodate Li-ions, leaving all 16c octahedral sites unoccupied. So at lower Li-ions concentrations ($0.74 < x < 1.015$), a two-phase transition occurs between octahedral and tetrahedral double-site occupation and tetrahedral single-site occupation. In this process, some Li-ions are fully extracted from octahedral sites and part Li-ions are also extracted from tetrahedral sites simultaneously, indicating a co-extraction process. After this stage ($x < 0.74$), Li ions only redistribute in 8a tetrahedral sites, which is the same as the ordinary spinel LMO. Thus, the predicted delithiation process can be described by following formula 2, 3, and 4

$$\begin{aligned}&(\ )_{8a}[Li_{2.115}]_{16c}(Mn_{0.085})_T(Li_{0.335}Mn_{1.665})_O[O_4]_{32e} \rightarrow\\&(Li_x)_{8a}\left[Li_y\right]_{16c}Li_x(Mn_{0.085})_T(Li_{0.335}Mn_{1.665})_O[O_4]_{32e}\\&x+y=1.05\end{aligned} \tag{2}$$

$$\begin{aligned}&(Li_x)_{8a}\left[Li_y\right]_{16c}Li_x(Mn_{0.085})_T(Li_{0.335}Mn_{1.665})_O[O_4]_{32e} \rightarrow\\&(Li_z)_{8a}[\ ]_{16c}(Mn_{0.085})_T(Li_{0.335}Mn_{1.665})_O[O_4]_{32e}\\&x+y=1.05,\ z<1\end{aligned} \tag{3}$$

$$\begin{aligned}&(Li_z)_{8a}[Li_{2.2}]_{16c}(Mn_{0.085})_T(Li_{0.335}Mn_{1.665})_O[O_4]_{32e} \rightarrow\\&(\ )_{8a}[\ ]_{16c}(Mn_{0.085})_T(Li_{0.335}Mn_{1.665})_O[O_4]_{32e}\ \ z<1\end{aligned} \tag{4}$$

Voltage profile of $Li_{2.115}(Mn_{0.085})_T(Li_{0.335}Mn_{1.665})_OO_4$ electrode at 0 K then can be determined using the following equation

$$\begin{aligned}&\bar{V}(x_2-x_1)=\\&-\frac{1}{x_2-x_1}\left(\begin{aligned}&E\left[Li_{x_2}(Mn_{0.085})_T(Li_{0.335}Mn_{1.665})_OO_4\right]-\\&E\left[Li_{x_1}(Mn_{0.085})_T(Li_{0.335}Mn_{1.665})_OO_4\right]\end{aligned}\right)-E[Li]\end{aligned} \tag{5}$$

where $\bar{V}(x_2-x_1)$ is the average voltage between separated phases $Li_{x_1}(Mn_{0.085})_T(Li_{0.335}Mn_{1.665})_OO_4$ and $Li_{x_2}(Mn_{0.085})_T(Li_{0.335}Mn_{1.665})_OO_4$ with respect to Li metal anode. E(Li) is the Li energy and e is the electron charge. The discharge stage between $0 < x < 0.465$ has been discarded since the Li-ions can't be extracted in the experiment. For $1.015 < x < 2.115$, two plateaus (≈1.6 V) are observed with a small difference of 0.05 V due to possibly solid-solution like two-phase transition. At this stage, Li ions are extracted from 16c octahedral sites in full lithiation. The calculated average voltage is obviously lower than experimental value (≈1.9 V), which can be attributed to the antisite Mn after Li/Mn exchange occupies 8a tetrahedral sites. They are coplanar connection to adjacent 16c Li-ions, leading to strong electrostatic repulsion between Mn and Li-ions. The electrostatic repulsions cause Li-ions shifting off-center from 16c sites and elevates energy of system. The excess anti-position could raise superfluous energy change. With further delithiation ($0.74 < x < 1.015$), the voltage plateau is increased to 2.8 V. At this stage, evident two-phase transition undergoes a transition from double-site occupation to single-site occupation. At stage $0.465 < x < 0.74$, the two-phase transition occurs in 8a tetrahedral sites, the voltage is calculated to be 3.9 V, in good agreement with electrochemical experimental results.

The mechanism of the suppression of JT distortion in LMO-CD was further investigated. Our calculations show that the ratio of Mn^{3+} to Mn^{4+} in normal LMO is 8:8 but all Mn ions in $Li_{2.115}(Mn_{0.085})_T(Li_{0.335}Mn_{1.665})_OO_4$ are almost reduced to Mn^{3+}. For the spinel $LiMn_2O_4$ supercell, the lattice $a = b = 8.20$ and $c = 8.76$ Å, and the elongation along z-direction is evident and about 6.8% raised by JT effect Mn^{3+} in this supercell. As for $Li_{2.115}(Mn_{0.085})_T(Li_{0.335}Mn_{1.665})_OO_4$, the calculated lattice parameters of supercells are $a = 8.58$, $b = 8.16$, and $c = 5.30$ Å, as shown in **Table 1**. Thus the $Li_{2.115}(Mn_{0.085})_T(Li_{0.335}Mn_{1.665})_OO_4$ exhibits an anisotropy in lattice parameters other than elongating along the certain direction. The JT effect in spinel LMO originates from the orbital degeneracy of JT active Mn^{3+} ion with electronic configuration $t_{2g}{}^3e_g{}^1$. The JT inactive Mn^{4+} ion processes fully unoccupied e_g orbital with $t_{2g}{}^3e_g{}^0$ electronic configuration. The calculated projected densities of states (PDOS) can distinguish different electronic states of Mn^{3+} and Mn^{4+} ions evidently, as shown in **Figure 6**a,b. It can be found that e_g orbitals of Mn^{4+}

Table 1. Calculated structure parameters of stoichiometric $LiMn_2O_4$ and $Li_{2.115}(Mn_{0.085})_T(Li_{0.335}Mn_{1.665})_OO_4$.

	a [Å]	*b* [Å]	*c* [Å]	Volume [Å^3]
$LiMn_2O_4$	8.20(8)	8.20(8)	8.76(0)	590.24(1)
$Li_{2.115}(Mn_{0.085})_T$-$(Li_{0.335}Mn_{1.665})_OO_4$	8.58(6)	8.16(1)	8.30(0)	581.58(9)

are fully unoccupied. In contrast, the JT active Mn^{3+} ion has been split into occupied d_{z2} and unoccupied d_{x2-y2} states due to asymmetric charge distribution, and ≈1 eV splitting gap can be found in e_g states of Mn^{3+} ion. The corresponding Mn—O bond lengths of MnO_6 octahedron are also represented. The bond lengths along c direction of Mn^{3+} ion show evident elongation comparing with that of Mn^{4+} ion. Figure 6c shows the calculated PDOS of $Li_{2.115}(Mn_{0.085})_T(Li_{0.335}Mn_{1.665})_OO_4$ supercell. The e_g states of the Mn^{3+} ion exhibit significant differences, in which both d_{z2} and d_{x2-y2} are partially occupied and no gap between them. Thus, e_g states of Mn^{3+} ion in LMO-CD supercell maintain degeneracy due to comparatively homogeneous charge distribution in d_{z2} and d_{x2-y2} orbitals. The Mn—O bond lengths of MnO_6 in $Li_{2.115}(Mn_{0.085})_T(Li_{0.335}Mn_{1.665})_OO_4$ show a relatively homogeneous distribution of Mn^{3+}—O bond lengths, compared with the distinct disproportionation of Mn^{3+}—O bond lengths in normal LMO (Figure S10, Supporting Information). Therefore, JT vitalities of Mn^{3+} ions have been suppressed in $Li_{2.2}Mn_{1.75}Li_{0.25}O_4$ by introducing cationic disorder (excess Li and Li/Mn exchange). This can be attributed to the symmetry breaking of Mn arrangement by cationic disorder. In solid compounds, compared with individual JT centers, the cooperative

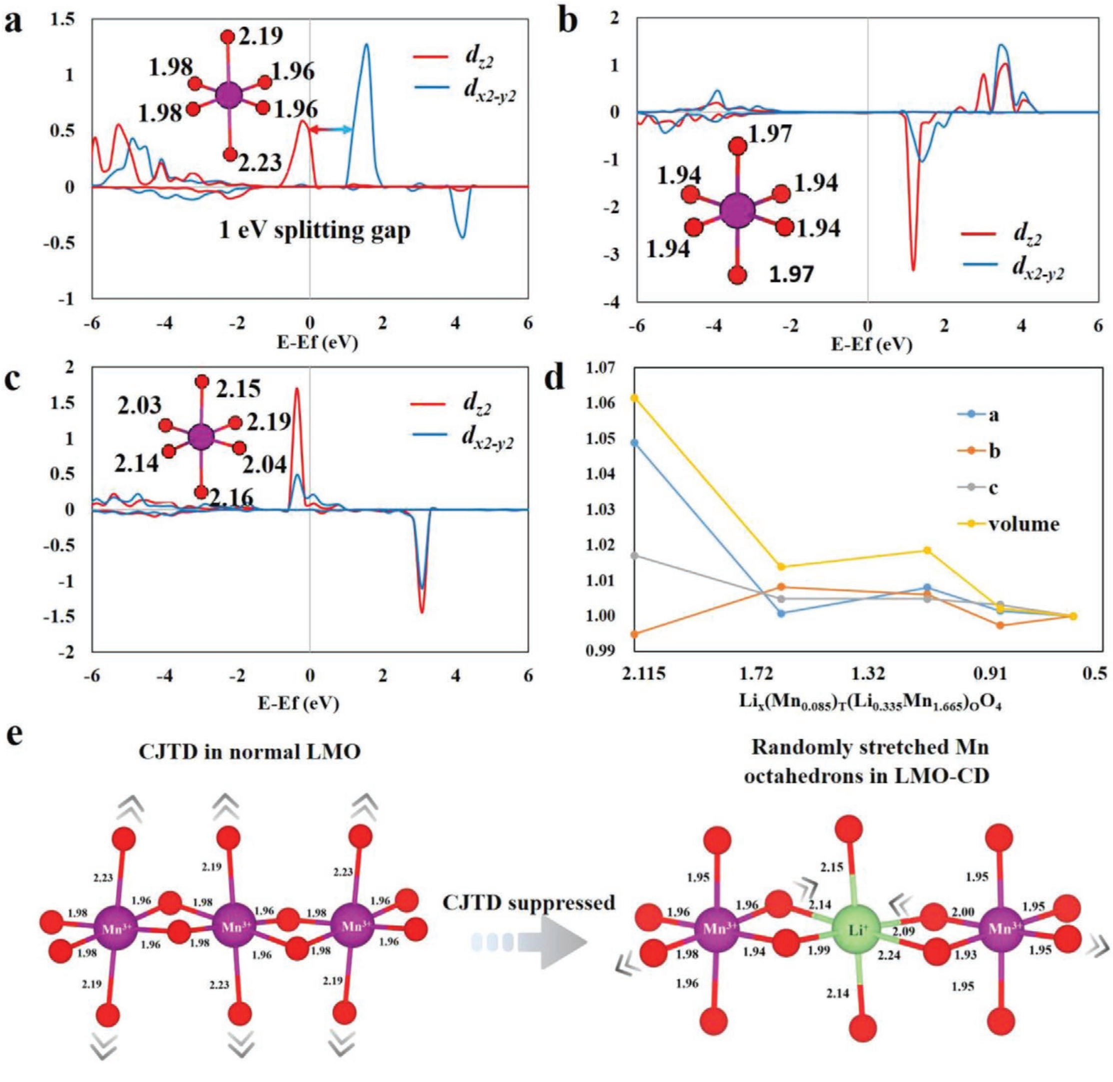

Figure 6. a) Projected density of states of Mn-e_g states for Mn^{3+} in normal spinel. b) Projected density of states of Mn-e_g states for Mn^{4+} in normal spinel. c) Projected density of states of Mn-e_g states for Mn^{3+} in LMO-CD. The insets represent corresponding MnO_6 octahedron marked with Mn—O bond lengths. The red and blue lines in the upper panel represent Mn-dz_2 and Mn-dx_2-y_2 orbitals, respectively. d) Structural changes during Li extraction in LMO-CD. The *y*-coordinate represents the ratio of change compared with the initial $Li_{2.115}(Mn_{0.085})_T(Li_{0.335}Mn_{1.665})_OO_4$. e) state of Mn^{3+} octahedrons when overlithiated for normal LMO and LMO-CD: Mn^{3+} octahedrons in normal LMO distort along *z* axis and generate huge structure change due to the cooperated JT effect while those in LMO-CD randomly stretched and counteract with each other to suppress the CJTD.

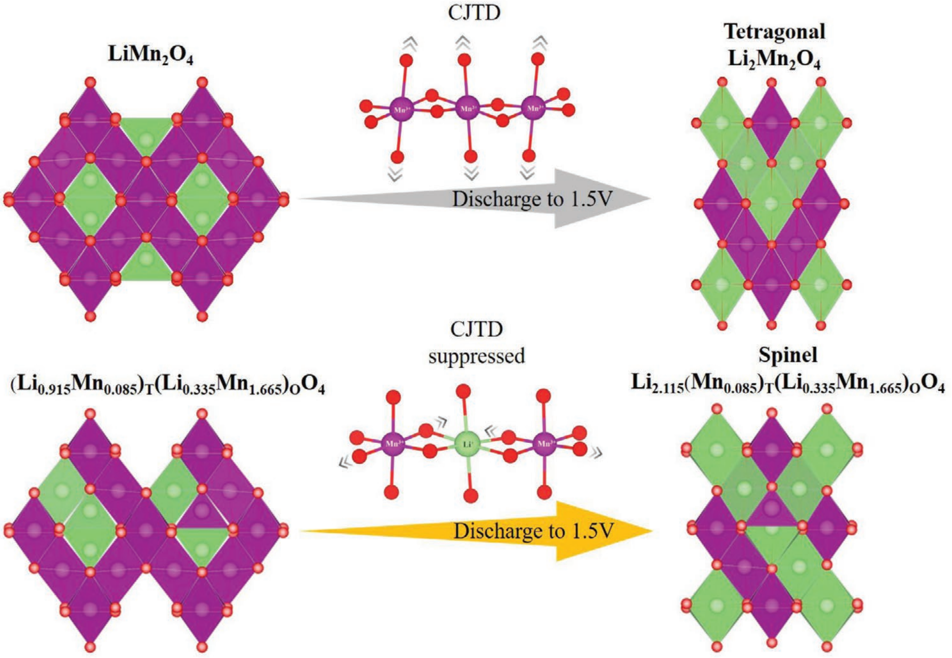

Figure 7. Schematic of the suppression process of the cooperative Jahn–Teller distortion in LMO-CD compared with normal LMO.

Jahn–Teller distortion (CJTD) referring to the correlation of distortions arising from individual JT centers would result in the elongations of $Mn^{3+}O_6$ octahedrons along a uniform direction and is more detrimental to the crystal structure (Figure 6e).[15] In our synthesized LMO-CD, excess Li and Li/Mn anti-position reduce the cubic symmetry *Fd*-3*m* of spinel LMO to a very low symmetry, so the correlation of individual active Mn^{3+} centers is disrupted, and the elongations of $Mn^{3+}O_6$ octahedrons can't follow a uniform direction but even offset with each other (Figure 6e). The equalization of d_{z2} and d_{x2-y2} orbitals of Mn^{3+} also stabilizes structural changes during redox between Mn^{3+} and Mn^{4+} since Mn—O bonds of these Mn^{3+} ions can smoothly transit to Mn^{4+} ions without drastic changes of bond lengths and JT stress. Figure 6d shows the calculated structural changes with Li extraction for $Li_{2.115}(Mn_{0.085})_T(Li_{0.335}Mn_{1.665})_OO_4$, and the small and anisotropic structural changes are in accordance with the experimental results and indicate.

Based on all the above discussions, we can summarize the CJTD suppression mechanism by cationic disordering in **Figure 7**. On the over-lithiated state, normal LMO will experience a tetragonal phase transition because of the serious CJTD arising from individual JT centers, leading to uniform $Mn^{3+}O_6$ octahedron stretching along c axis. While for LMO-CD, with Li substitution of Mn and Li/Mn exchange, the spinel structure framework can be well retained due to the suppressed CJTD. Because the Li/Mn exchange and Li substitution can break the symmetry of Mn^{3+} arrangements, and the correlation of individual active Mn^{3+} centers is disrupted. These random distortions would inhibit the elongations of $Mn^{3+}O_6$ octahedrons along a uniform direction but even make them counteract with each other. The suppressed CJTD finally leads to the relatively homogeneous distribution of Mn^{3+}—O bond lengths, compared with the significant disproportionation of Mn^{3+}—O bond lengths in normal LMO (Figure S10, Supporting Information).

3. Conclusions

In conclusion, using experiments combined with extensive ab initio calculations, we access the double capacity beyond one lithium intercalation with good reversible cycling stability in microsized spinel LMO by cationic disordering (excess Li at Mn sites and Li/Mn exchange). We prove that the cationic disorder (excess Li at Mn sites and Li/Mn exchange) can intrinsically suppress the CJTD of $Mn^{3+}O_6$ octahedrons and inhibit the Mn^{3+} disproportionation in the spinel bulk. The cationic disordering can break the symmetry of Mn arrangements to disrupt the correlation of individual JT centers, and these random distortions would inhibit the elongations of $Mn^{3+}O_6$ octahedrons along a uniform direction but even make them counteract with each other. Due to the suppressed CJTD in LMO-CD, a high reversible double capacity (≈240 mAh g^{-1}) with good cycling stability at a voltage window of 1.5 to 4.8 V is obtained, which can be attributed to that the original octahedral vacancies in spinel LMO are activated and can serve as extra Li-ion storage sites. The above findings provide useful guidelines on the future development of LMO based LIBs with higher capacity and longer life by suppressing the CJTD.

4. Experimental Section

Material Synthesis: The manganese spinel with cationic disordering was synthesized via a molten-salt method. Manganese dioxide and 5 wt% acetylene black as a reductant were mixed uniformly using mortar and pestle. Then 0.5 g of the mixture was added to lithium salt composing with 4.4 g $LiNO_3$ and 0.6 g LiCl, and mixed them thoroughly.

The mixture was next calcined in the air at 460 °C for 8 h in a covered alumina crucible. The resulting powder was washed thoroughly by suction filtration using deionized water and ethyl alcohol to remove the residual $LiNiO_3$ and LiCl. The lithium rich manganese spinel was obtained after dried at 80 °C overnight. $LiMn_2O_4$ was prepared by a solid-state method. Stoichiometric amounts of Li_2CO_3 and $MnCO_3$ were thoroughly mixed using a ball-milling machine. $LiMn_2O_4$ powder was obtained after calcining the mixture at 750 °C in the air for 8 h.

Morphology and Structure Studies: The morphology of as-prepared sample was investigated by field-emission scanning electron microscopy (ZEISS SUPRA55, Carl Zeiss) and high-resolution transmission electron microscopy (JEM-3200FS, JEOL). X-ray powder diffraction (XPD) was carried out with an X-ray diffractometer (D8 advance, Bruker) in the 2θ range from 10° to 80°, and the structure Rietveld was performed by Fullprof. The chemical formula was determined by inductively coupled plasma optical emission spectrometry (ICP-OES).

Preparation of Coin Cells: The cathode was prepared by mixing the active material, acetylene black and polyvinylidene fluoride (PVDF) in a weight ratio of 8:1:1. The N-methylpyrrolidone (NMP) was used as the solvent to form a slurry. The slurry was coated onto an aluminum foil using a 100 µm height blade and then dried at 80 °C for 6 h. The cathode was punched into 10 mm diameter disks with the active material loading around 1.5 mg and then dried in a vacuum oven for 12 h. 2025-type coin cells were assembled in an Argon-filled glove box, in which oxygen and water content were less than 0.01 ppm. Lithium metal and glass microfiber were used as the anode and the separator, respectively. The electrolyte was a solution containing $LiPF_6$ and addictive in EC/DMC.

Electrochemical Tests: The half cells were charged and discharged at different current densities in a voltage window of 1.5–4.8 V versus Li/Li^+ in the NEWARE battery cycler at room temperature. Cyclic voltamograms (CV) were performed in the same voltage range at a scan rate of 0.1 mV s^{-1}.

Calculation Methods: All calculations were performed using the plane-wave based spin-polarized density functional theory (DFT) method as implemented in the Vienna ab initio simulation package (VASP).[16] The projector augmented wave approach was used to describe the interaction between the core and valence electrons.[17] The Perdew–Burke–Ernzerhof (PBE) exchange-correlation function of the generalized-gradient approximations (GGA) was used for ionic position optimization and electronic structure calculation.[18] A cutoff energy of 500 eV for the plane wave basis set was used in all calculations, and the k-point sampling with a $3 \times 3 \times 3$ mesh was used to geometric optimization. All configurations have reached a convergence threshold of 0.01 eV Å^{-1} in force.[19] It should be noticed that the experimental voltage can be realized only by PBE without U. The usual U value 3.8 or 4.2 eV used in $LiMn_2O_4$ calculations can't repeat the experimental average voltage 2.8 V and overestimates the average voltage to 3.5 eV.[19,20]

Supporting Information

Supporting Information is available from the Wiley Online Library or from the author.

Acknowledgements

C.Z. and Z.H. contributed equally to this work. This work was financially supported by National Key R&D Program of China (2016YFB0700600), Soft Science Research Project of Guangdong Province (No. 2017B030301013), and Shenzhen Science and Technology Research Grant (ZDSYS201707281026184)

Conflict of Interest

The authors declare no conflict of interest.

Keywords

batteries, doping, Jahn–Teller distortion, lithium-ion storage, spinel

Received: January 28, 2020
Revised: June 29, 2020

[1] a) J. M. Tarascon, M. Armand, *Nature* **2001**, *414*, 359; b) Z. Yang, J. Zhang, M. C. Kintner-Meyer, X. Lu, D. Choi, J. P. Lemmon, J. Liu, *Chem. Rev.* **2011**, *111*, 3577.

[2] a) B. L. Ellis, K. T. Lee, L. F. Nazar, *Chem. Mater.* **2010**, *22*, 691; b) O. K. Park, Y. Cho, S. Lee, H.-C. Yoo, H.-K. Song, J. Cho, *Energy Environ. Sci.* **2011**, *4*, 1621; c) E. Hosono, T. Kudo, I. Honma, H. Matsuda, H. Zhou, *Nano Lett.* **2009**, *9*, 1045; d) M. J. Lee, S. Lee, P. Oh, Y. Kim, J. Cho, *Nano Lett.* **2014**, *14*, 993; e) V. Manev, B. Banov, A. Momchilov, A. Nassalevska, *J. Power Sources* **1995**, *57*, 99; f) Y. Huang, Y. Dong, S. Li, J. Lee, C. Wang, Z. Zhu, W. Xue, Y. Li, J. Li, *Adv. Energy Mater.* **2020**, 2000997, https://doi.org/10.1002/aenm.202000997.

[3] a) T. Ohzuku, J. Kato, K. Sawai, T. Hirai, *J. Electrochem. Soc.* **1991**, *138*, 2556; b) M. M. Thackeray, W. I. F. David, P. G. Bruce, J. B. Goodenough, *Mater. Res. Bull.* **1983**, *18*, 461.

[4] a) M. M. Thackeray, *Prog. Solid State Chem.* **1997**, *25*, 1; b) M. M. Thackeray, A. Dekock, M. H. Rossouw, D. Liles, R. Bittihn, D. Hoge, *J. Electrochem. Soc.* **1992**, *139*, 363.

[5] a) T. Liu, A. Dai, J. Lu, Y. Yuan, Y. Xiao, L. Yu, M. Li, J. Gim, L. Ma, J. Liu, C. Zhan, L. Li, J. Zheng, Y. Ren, T. Wu, R. Shahbazian-Yassar, J. Wen, F. Pan, K. Amine, *Nat. Commun.* **2019**, *10*, 4721; b) J. Lu, C. Zhan, T. Wu, J. Wen, Y. Lei, A. J. Kropf, H. Wu, D. J. Miller, J. W. Elam, Y. K. Sun, X. Qiu, K. Amine, *Nat. Commun.* **2014**, *5*, 5693; c) C. Zhan, J. Lu, A. Jeremy Kropf, T. Wu, A. N. Jansen, Y. K. Sun, X. Qiu, K. Amine, *Nat. Commun.* **2013**, *4*, 2437.

[6] a) Q. Tong, Y. Yang, J. Shi, J. Yan, L. Zheng, *J. Electrochem. Soc.* **2007**, *154*, A656; b) B. L. He, W. J. Zhou, Y. Y. Liang, S. J. Bao, H. L. Li, *J. Colloid Interface Sci.* **2006**, *300*, 633; c) M. Takahashi, T. Yoshida, A. Ichikawa, K. Kitoh, H. Katsukawa, Q. Zhang, M. Yoshio, *Electrochim. Acta* **2006**, *51*, 5508; d) J. M. Amarilla, K. Petrov, F. Pico, G. Avdeev, J. M. Rojo, R. M. Rojas, *J. Power Sources* **2009**, *191*, 591.

[7] S. Li, K. Zhu, D. Zhao, Q. Zhao, N. Zhang, *Ionics* **2019**, *25*, 1991.

[8] a) Y. Xie, Y. Jin, L. Xiang, *ACS Appl. Mater. Interfaces* **2019**, *11*, 14796; b) G. Xu, Z. Liu, C. Zhang, G. Cui, L. Chen, *J. Mater. Chem. A* **2015**, *3*, 4092.

[9] M. Lin, S. H. Wang, Z. L. Gong, X. K. Huang, Y. Yang, *J. Electrochem. Soc.* **2013**, *160*, A3036.

[10] J. Lu, Y. L. Chang, B. H. Song, H. Xia, J. R. Yang, K. S. Lee, L. Lu, *J. Power Sources* **2014**, *271*, 604.

[11] a) S. H. Kang, J. B. Goodenough, L. K. Rabenberg, *Chem. Mater.* **2001**, *13*, 1758; b) H. K. Noh, H.-S. Park, H. Y. Jeong, S. U. Lee, H.-K. Song, *Angew. Chem.* **2014**, *126*, 5159; *Angew. Chem., Int. Ed.* **2014**, *53*, 5059.

[12] F. Jiao, J. Bao, A. H. Hill, P. G. Bruce, *Angew. Chem.* **2008**, *120*, 9857; *Angew. Chem., Int. Ed.* **2008**, *47*, 9711.

[13] a) R. J. Gummow, A. D. Kock, M. M. Thackeray, *Solid State Ionics* **1994**, *69*, 59; b) A. Yamada, *J. Solid State Chem.* **1996**, *122*, 160.

[14] a) H. Berg, H. Rundlöv, J. O. Thomas, *Solid State Ionics* **2001**, *144*, 65; b) H. Berg, J. O. Thomas, *Solid State Ionics* **1999**, *126*, 227.

[15] a) G. A. Gehring, K. A. Gehring, *Rep. Prog. Phys.* **1975**, *38*, 1; b) J. B. Goodenough, *Annu. Rev. Mater. Sci.* **1998**, *28*, 1; c) X. Li, X. H. Ma, D. Su, L. Liu, R. Chisnell, S. P. Ong, H. L. Chen, A. Toumar, J. C. Idrobo, Y. C. Lei, J. M. Bai, F. Wang, J. W. Lynn, Y. S. Lee, G. Ceder, *Nat. Mater.*

2014, *13*, 586; d) T. Amriou, B. Khelifa, H. Aourag, S. M. Aouadi, C. Mathieu, *Mater. Chem. Phys.* **2005**, *92*, 499; e) A. Rougier, C. Delmas, A. V. Chadwick, *Solid State Commun.* **1995**, *94*, 123.
[16] G. Kresse, J. Hafner, *Phys. Rev. B* **1993**, *47*, 558.
[17] P. E. Blochl, *Phys. Rev. B* **1994**, *50*, 17953.
[18] J. P. Perdew, K. Burke, M. Ernzerhof, *Phys. Rev. Lett.* **1996**, *77*, 3865.
[19] A. Vasileiadis, B. Carlsen, N. J. J. de Klerk, M. Wagemaker, *Chem. Mater.* **2018**, *30*, 6646.
[20] W. Xiao, C. Xin, S. Li, J. Jie, Y. Gu, J. Zheng, F. Pan, *J. Mater. Chem. A* **2018**, *6*, 9893.